JGR Solid Earth

RESEARCH ARTICLE
10.1029/2022JB026114

Tracking a Pyroclastic Density Current With Seismic Signals at Mt. Etna (Italy)

Leighton M. Watson[1], Andrea Cannata[2,3], and Daniele Andronico[3]

[1]School of Earth and Environment, University of Canterbury, Christchurch, New Zealand, [2]Dipartimento di Scienze Biologiche, Geologiche e Ambientali - Sezione di Scienze della Terra, Università degli Studi di Catania, Catania, Italy, [3]Istituto Nazionale di Geofisica e Vulcanologia, Osservatorio Etneo – Sezione di Catania, Catania, Italy

Key Points:

- Pyroclastic density currents (PDCs) are hazardous volcanic flows that generate seismic and acoustic signals
- By considering the attenuation of seismic amplitudes with distance, seismic signals can be used to track PDCs
- Seismic signals can be used to track PDCs and other surficial mass movements in real-time

Supporting Information:

Supporting Information may be found in the online version of this article.

Correspondence to:

L. M. Watson,
leighton.watson@canterbury.ac.nz

Citation:

Watson, L. M., Cannata, A., & Andronico, D. (2023). Tracking a pyroclastic density current with seismic signals at Mt. Etna (Italy). *Journal of Geophysical Research: Solid Earth*, *128*, e2022JB026114. https://doi.org/10.1029/2022JB026114

Received 23 NOV 2022
Accepted 20 FEB 2023

Author Contributions:

Conceptualization: Leighton M. Watson
Data curation: Leighton M. Watson, Andrea Cannata, Daniele Andronico
Formal analysis: Leighton M. Watson, Andrea Cannata
Funding acquisition: Leighton M. Watson
Investigation: Leighton M. Watson, Andrea Cannata, Daniele Andronico
Methodology: Leighton M. Watson, Andrea Cannata
Project Administration: Leighton M. Watson
Resources: Leighton M. Watson
Software: Leighton M. Watson

Abstract Pyroclastic density currents (PDCs) are dangerous flows of volcanic rock and gas that are the most deadly proximal volcano hazard. There is significant interest in better understanding PDC dynamics, however, they are challenging to study due to their extreme hazard, unpredictable occurrence, and because complex internal dynamics are obscured by visually opaque clouds of ash. PDCs exert forces on Earth's surface and generate seismic waves. Here, we use seismic data recorded by the permanent monitoring network at Mt. Etna (Italy) to track the 11 February 2014 PDC at second-scale temporal resolution and calculate a maximum velocity of 76 m/s (274 km/hr). We identify multiple pulses and show that the late-stage source locations correspond with the mapped coarse-grained PDC deposits. High temporal and spatial resolution measurements of PDC movement from seismic data can be used to inform numerical modeling of PDC dynamics and aid in hazard assessment by improving our understanding of PDC flow paths. This work illustrates how seismic signals can be used to track surficial mass movements in real-time.

Plain Language Summary Pyroclastic density currents are deadly, very often sudden and unexpected, fast-moving clouds of hot volcanic gas, ash, and rock. They travel extremely quickly and are very hazardous. As the pyroclastic density current (PDC) flows downslope, it pushes onto Earth's surface producing seismic waves. From these seismic signals, we can track the flow. We study a PDC that occurred at Mt. Etna (Italy) on 11 February 2014. Using the seismic signals, we track the flow and calculate a velocity of 274 km/hr. This work shows how seismic signals can be used to track moving flows, which has applications for understanding complex flow dynamics and real-time monitoring.

1. Introduction

Pyroclastic density currents (PDCs) are hot mixtures of eruption-derived particles and gas that move laterally along the ground and are driven by negative buoyancy. Due to their mobility, rapid velocities, and high temperatures, PDCs are the most hazardous proximal volcanic phenomena and are responsible for over 50% of volcanic-related fatalities (Lube et al., 2019). PDCs have been observed to travel distances of over 100 km (Druitt, 1998; Valentine et al., 1989), flow over substantial (>1,000 m) topographic barriers (Fisher et al., 1993; Woods et al., 1998), and reach speeds in excess of 500 km/hr (Moore & Rice, 1984) and temperatures near to (Cioni et al., 2004) or in excess of 400°C (Ripepe et al., 2009). PDCs are characterized by a two-layer structure with a dense basal flow overlain by a dilute suspended region (Dufek, 2016).

Due to their hazardous nature, there is a pressing need to better understand PDC dynamics. However, they are challenging to observe directly as they occur infrequently in remote and inhospitable volcanic environments. Direct visual observations can usually only be made of the outer shell of the flow with the complex internal dynamics obscured by visually opaque fluid (Dufek, 2016). Therefore, most of our understanding of these multiphase, turbulent flows comes from laboratory studies (e.g., Breard & Lube, 2017; Lube et al., 2019; Roche et al., 2010; Wilson, 1980), numerical models (e.g., Benage et al., 2016; Doronzo et al., 2010; Dufek & Bergantz, 2007a, 2007b; Dufek et al., 2009; Fisher, 1979; Neri et al., 2003; Valentine & Wohletz, 1989), and geological observations of PDC deposits (e.g., Cole et al., 2002; Fisher, 1966; Gurioli et al., 2010; Pollock et al., 2019; Smith, 1960; Sparks et al., 1973; Walker, 1971). Geological deposits associated with the dense basal flow are initially controlled by the pre-existing topography during the turbulent/granular flow stage of a PDC, which evolves to a fluidized flow stage due to the gradual flattening of the slope, while deposits associated with the dilute suspended region are typically dispersed over a larger area (Fujii & Nakata, 1999; Takahashia & Tsujimoto, 2000).

Validation: Leighton M. Watson, Daniele Andronico
Visualization: Leighton M. Watson
Writing – original draft: Leighton M. Watson, Andrea Cannata, Daniele Andronico
Writing – review & editing: Leighton M. Watson, Andrea Cannata, Daniele Andronico

By displacing atmospheric air and exerting forces on Earth's surface, PDCs generate acoustic waves in the atmosphere (termed infrasound as the waves are predominately at frequencies <20 Hz, which is below the threshold of human hearing) and seismic waves in the solid earth (e.g., De Angelis et al., 2007; Delle Donne et al., 2014; Ripepe et al., 2009; Uhira et al., 1994). Geophysical observations (infrasound and seismic) can be made at safe distances from PDC activity and can provide high-resolution information about PDC dynamics (see Allstadt et al., 2018 for a review of infrasound and seismic signals from surficial mass movements at volcanoes including PDCs).

Previous studies have used seismic signals, along with other data sources such as infrasound and visual and thermal video footage, to detect, locate, and characterize PDC activity. Seismic signals associated with PDCs are characterized as emergent, waxing, and waning signals with extended durations (>10 s) and frequencies of 1–10 Hz (Calder et al., 2002). Yamasato (1997) analyzed infrasonic, seismic, and video records of PDCs at Unzen volcano (Japan) produced by collapse of the dacite lava dome. Through comparison with video footage, Yamasato (1997) located the source of the infrasound signals to near the front of the flow, suggesting that fragmentation of coarse-grained pyroclasts and large volcanic blocks predominantly occurs near the front of the PDC. Zobin (2018) and Zobin et al. (2009) studied seismic signals from PDCs at Volcan de Colima (Mexico) and, similar to Yamasato (1997), showed that the main part of the seismic signal is generated by the fluidized flow stage of the PDC. Zobin et al. (2009) also demonstrated that the seismic signals are similar for PDCs generated by the collapse of a lava dome or the collapse of an eruption column. DeRoin et al. (2012) compared seismic data with visual observation at Augustine Volcano (Alaska) to calculate PDC velocities and demonstrated that seismic observations can "provide hazard monitoring information on directions, durations, sizes, and run-out distances." Calvari et al. (2020) studied eruptive activity at Stromboli (Italy) and recorded seismic signals of PDCs entering the sea. Jolly et al. (2002) used seismic amplitude information to locate PDCs at Soufriere Hills volcano (Montserrat), which is similar to the methodology used in this work, and were able to track PDC movement downslope.

Due to the hazard posed by PDCs, there is a pressing need to improve monitoring capabilities. In this study, we analyze seismic signals recorded during a PDC that occurred at Mt. Etna (Italy) on 11 February 2014. By considering the amplitude decay of seismic signals with distance from the source, we locate the sources of the seismic signals, track the source location through time, and compare with mapped PDC deposits (Andronico et al., 2018). This methodology provides unprecedented spatial and temporal resolution of PDC dynamics, which has implication for understanding PDC dynamics and depositional processes. We demonstrate that this method could be used to track PDCs in real-time, which has important implications for monitoring surficial mass movements at volcanoes. We examine how the results change with a variable number of seismic stations to illustrate how this analysis could be applied at other less well-monitored volcanoes.

2. PDCs at Mt. Etna

Mt. Etna is a volcano on the eastern coast of Sicily (Italy) that is characterized by persistent degassing and frequent eruptions. Small-volume PDCs have been observed at Mt. Etna multiple times in recent years. Behncke (2009) documented eight instances of PDC activity at Mt. Etna between 1986 and 2007 and identified four different generation mechanisms: (a) collapse of pyroclastic fountains, (b) phreatomagmatic explosions due to the mixing of lava with wet rock or (c) thick snow, and (d) failure of lava domes growing over the rims of the summit craters. The maximum runout distance observed was 1.5 km for a PDC from the base of the Southeast Crater (SEC) on 24 November 2006 (Behncke, 2009; Norini et al., 2009). Due to dozens of paroxysmal episodes (Andronico et al., 2021), rapid growth of SEC since 2006 and the New Southeast Crater (NSEC) since 2011 has resulted in an increasing number of PDCs and landslides (Andronico et al., 2018; INGV-OE, 2020a, 2022).

On 11 February 2014, a PDC was produced by failure of 0.82–1.29 × 10^6 m^3 of unstable hot rock from the lower-eastern flank of NSEC (Andronico et al., 2018). The surveillance cameras of the Instituto Nazionale di Geofisica e Vulcanologia - Osservatorio Etneo (INGV–OE) showed a weak reddish ash emission starting at 06:06:50 GMT from an active effusive vent area located a few hundreds of meters below the summit of the SEC. This emission preceded the ash cloud generated by the formation and descent of the PDC down the NSEC slopes by about 20 s. Strombolian activity at NSEC was ongoing during and after the flow event. The flow traveled 2.3 km from the source (INGV, 2014), which is the longest PDC runout witnessed at Mt. Etna, reached temperatures of up to 750°C, and had an average speed of >40 m/s (144 km/hr; Andronico et al., 2018). The PDC deposits

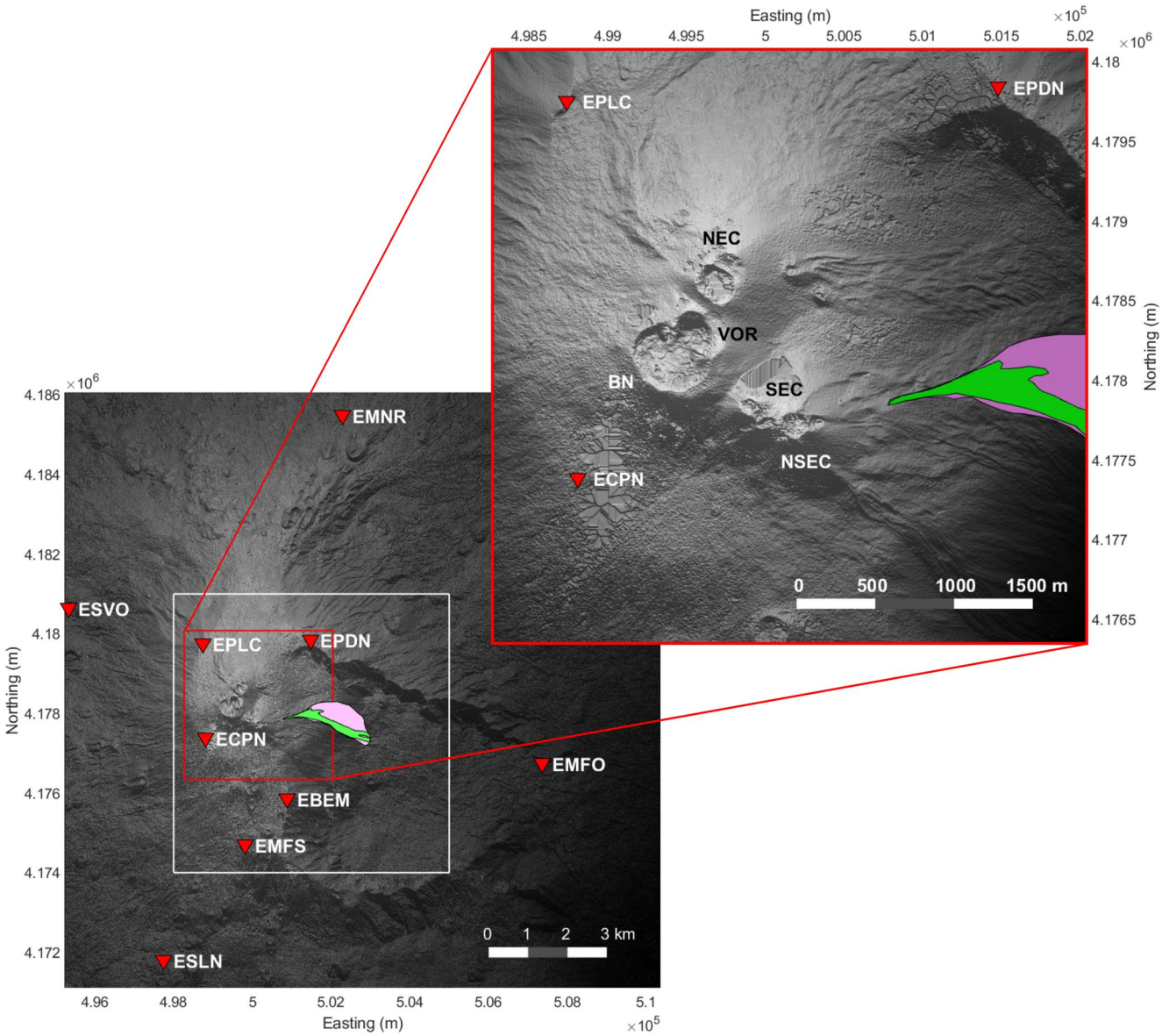

Figure 1. Digital elevation model of Mt. Etna (Ganci et al., 2019) obtained from tri-stereo Pléiades data acquired on 18 December 2015. Eastings and northings are in UTM Zone 33°N. Red triangles indicate the location of seismometers while the shaded purple and green regions show the fine-grained and coarse-grained pyroclastic density current deposits, respectively, mapped by Andronico et al. (2018). The white box indicates the search area for the seismic source locations. The red box shows the crater area; see inset in the upper right (NEC, North-East Crater; VOR, Voragine; BN, Bocca Nuova; SEC, South-East Crater; NSEC, New South-East Crater).

had a volume of 0.39–0.92 × 10^6 m^3 (Andronico et al., 2018) with a thickness of up to 2–3 m (INGV, 2014). For more details about the generation mechanism and geological deposits of the PDC, see Andronico et al. (2018).

Since 2014, the intense and frequent paroxysmal activity has led the NSEC to merge with the SEC forming a single, large cone named SEC in November 2020 (INGV-OE, 2020b), which retains the propensity to produce PDCs, especially during ongoing lava fountaining episodes. The most striking recent PDC events occurred on 13–14 December 2020 and 10 February 2022 (INGV-OE, 2020a, 2022).

3. Data

The INGV-OE maintains a network of seismic and infrasound sensors around the summit of Mt. Etna, along with several visual and thermal cameras. Here, we focus on nine seismic stations with locations shown in Figure 1.

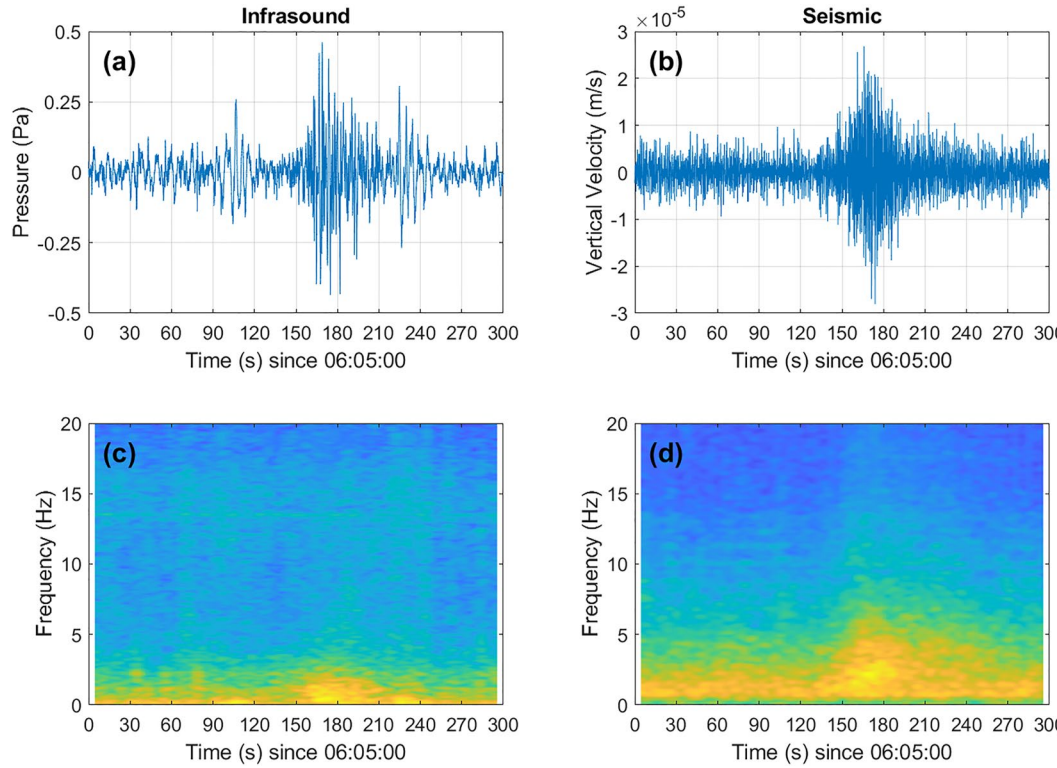

Figure 2. Infrasound and seismic data recorded at station EMFO. (a) Infrasound time series. (b) Vertical velocity time series. (c) Infrasound spectrogram. (d) Seismic spectrogram. Spectrograms are calculated over 10 s sliding windows with 90% overlap. Warm colors (yellow) indicate high amplitude and cool colors (blue) indicate low amplitudes.

Each station is equipped with a broadband three-component Nanometrics Trillium 40 s seismometers sampling at 100 Hz. Stations are within 1–8 km of the summit. Each station is also equipped with a GRASS 40AN microphone with a flat response with sensitivity of 50 mV/Pa in the frequency range of 0.3–20,000 Hz, except for ECPN and ESLN which had Monacor MC 2005 condenser microphones with a sensitivity of 80 mV/Pa in the 1–20 Hz infrasonic band in 2014. The infrasound microphones sample at 50 Hz (Cannata et al., 2013). The data is available at Larocca et al. (2023).

Figure 2 shows the time series and spectrogram for infrasound data and the vertical component of the seismic signal recorded at EMFO. The PDC signal is visible between 120 and 240 s since 06:05:00 UTM and is characterized by an emergent onset and extended duration of ~2 min. This is similar to geophysical observations of other surficial mass movements (e.g., Allstadt et al., 2018). The seismic signal from the PDC and the background noise/volcanic activity has more high-frequency components than the infrasound signal does. While the seismic signal of the PDC is visible at multiple stations (Figure 3), the infrasound signal from the PDC is only visible at EMFO. This may be because the PDC propagates in the direction of EMFO and preferentially excites acoustic radiation in that direction. The PDC occurs on the eastern flank of the volcano and topographic scattering and reflections may prevent the acoustic waves from propagating to the stations on the western flank. In addition, the summit stations are more exposed and are closer to the active summit vents meaning that, for these stations, the PDC infrasound signal may be overwhelmed by wind noise or sound from ongoing Strombolian activity at the vent. Hence, we focus our analysis on the seismic data shown in Figure 3.

4. Methods

Seismic source locations before, during, and after the PDC are determined by considering the decay of seismic amplitude with distance from the source. This approach has been previously used to locate tremor sources at Piton de la Fournaise (Battaglia et al., 2005) and Mt. Etna (Cannata et al., 2013; Di Grazia et al., 2006), which, like the PDC signal considered here, do not have clear first arrivals. More recently, this method has also been used to locate seismic sources in debris flows (Walter et al., 2017).

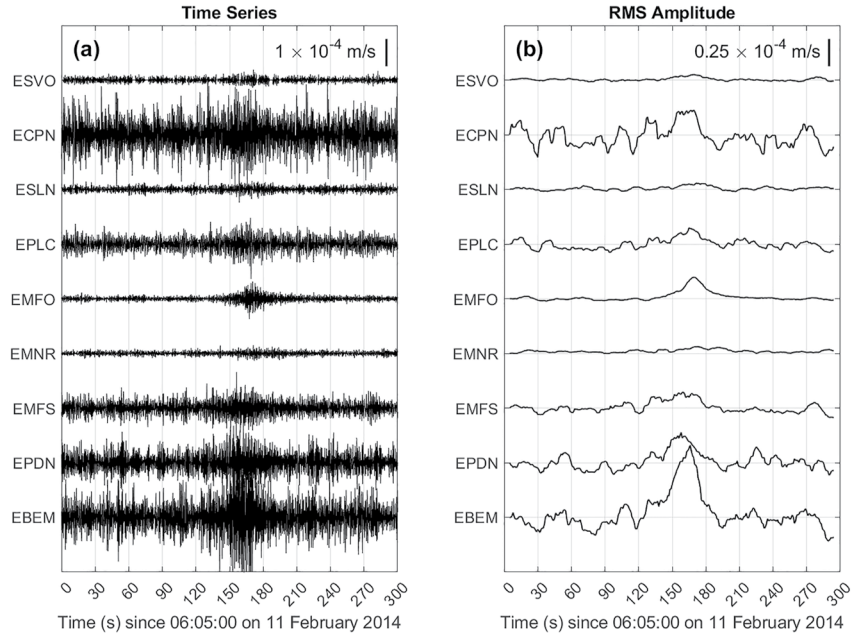

Figure 3. (a) Signal and (b) root mean square amplitude (RMS) for the vertical component of the seismic data recorded at nine seismic stations (station locations are shown in Figure 1). RMS amplitude is calculated on 10 s sliding windows with 90% overlap between windows.

The seismic amplitude, A, decays with source-receiver distance, r, according to:

$$A(f, r) = A_0(f)\, r^{-b} e^{-\alpha r} \tag{1}$$

where f is the frequency, b is the exponent, which is 0.5 for surface waves and 1 for body waves, A_0 is the amplitude at the source, and α is the frequency-dependent absorption coefficient defined as follows:

$$\alpha = \frac{\pi f}{Qc} \tag{2}$$

where Q is the ray-path-averaged quality factor and c is the wave speed.

Equation 1 can be linearized by taking the natural logarithm of both sides (Cannata et al., 2013, 2010; Di Grazia et al., 2006):

$$ln\, A_i + \alpha r_i = ln\, A_0 - b\, ln\, r_i \tag{3}$$

where A_i is the RMS amplitude at the ith station (Figure 3b) and r_i is the corresponding source-receiver distance. In this analysis, we ignore site effects as a year-long study of volcano tremor at Mt. Etna by Cannata et al. (2010) showed that site effects do not significantly influence the source locations. Furthermore, Cannata et al. (2010) and Patanè et al. (2008) examined different values of α and observed that the best fit was achieved with low values between 0 and 0.02. For simplicity, and because the attenuation factor does not have a large influence on source locations (Battaglia et al., 2005), we set $\alpha = 0$. Hence, Equation 3 is simplified to:

$$ln\, A_i = ln\, A_0 - b\, ln\, r_i \tag{4}$$

By viewing $ln\, A_0$ and b as the intercept and slope of a linear equation, respectively, the source location of the tremor can be determined by the goodness of the linear regression fit, R^2.

We perform a two-dimensional (2D) grid search over possible source locations with the nodes constrained to the topographic surface. We focus on a 7 km by 7 km region around the summit vents and mapped PDC deposits (Figure 1) using a grid spacing of 20 m, which corresponds to 350 grid points in each direction. The RMS amplitude is calculated on 10 s sliding windows with 90% overlap. Considering a seismic velocity in the shallow layers of 1,800 m/s, a 10 s window length means seismic signals can travel 18 km in this time. Using this window

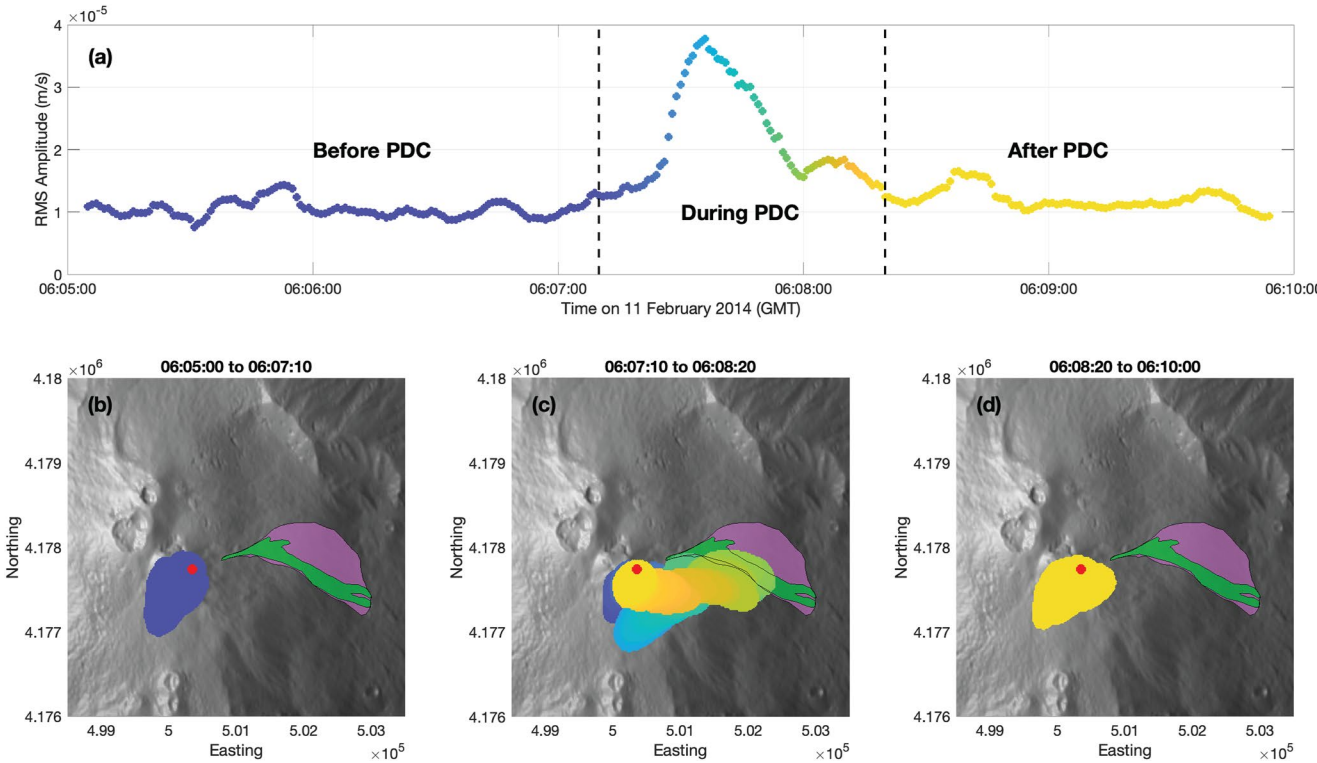

Figure 4. (a) Root mean square (RMS) amplitude recorded at station EBEM. (b–d) Seismic source location calculated from amplitude decay with distance (Equation 4) for before, during, and after the pyroclastic density current (PDC), respectively. Source locations are color-coded by time as shown in (a). The purple and green shaded regions show the fine and coarse-grained PDC deposits, respectively, mapped in Figure 6 of Andronico et al. (2018). Red circles indicate the location of NSEC, which is the origin of the distances shown in Figure 5. Vertical black dashed lines in (a) indicate the different phases of activity.

length means that signals generated by the same source should be observed by all of the analyzed stations within the window.

The 2D grid search is performed in time steps of one second between 06:05:00 and 06:10:00 GMT on 11 February 2014. This results in a grid search over approximately 36 million grid points. Grid points are classified as sources when the R^2 value is within 99% of the maximum R^2 value at that time step (Cannata et al., 2013). The calculated source locations are similar for $b = 1$, $b = 0.5$, and for a variable exponent solution, although the surface wave solution ($b = 0.5$) is generally further to the south and east. In this work, we use $b = 1$ as it resulted in higher R^2 values than for $b = 0.5$ (Figure S1 in Supporting Information S1). The RMS amplitude is calculated from the vertical component of the seismic signal. Figure S2 in Supporting Information S1 shows a comparison of the source locations calculated from the vertical component and from the vectorial combination of the three components of velocity.

5. Results

The seismic source locations are shown in Figure 4 and are divided into before (06:05:00 to 06:07:10), during (06:07:10 to 06:08:20), and after (06:08:20 to 06:10:00) the PDC. Before and after the PDC (Figures 4b and 4d), seismic sources are located at the summit around SEC and NSEC. During the PDC, the seismic source locations move downslope and are elongated in the flow direction to the east (Figure 4c). The PDC has multiple pulses (see Movie M1) with the final pulse of source locations overlapping the coarse-grained PDC deposits mapped by Andronico et al. (2018).

Figure 5 shows the easting and northing components of the mean seismic source location as a function of time. Before the PDC, the source locations oscillate but are generally within 500 m to the west and south of the NSEC. During the PDC, the source location moves to the east and south before switching to moving to the north with an increased velocity to the east at 06:07:35. After the PDC ends (after 06:08:20), the source locations move back to the south and west of the NSEC.

In order to estimate the PDC velocity, we fit a linear model to the easting and northing components during the main descent of the PDC (black dashed line in Figure 5a). The linear fit gives a velocity of 71 m/s (256 km/hr) in the

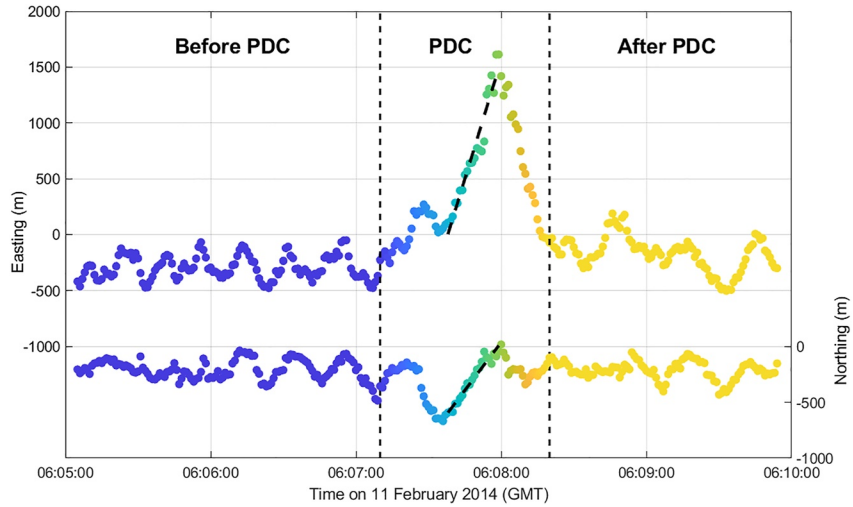

Figure 5. Mean easting (top line, left axis) and northing (bottom line, right axis) of the seismic source location. The origin is NSEC (Easting = 500,351 m, Northing = 4,177,740 m, UTM Zone 33°N), which is shown as the red circles in Figure 4. Black dashed lines show linear fit to the source location during the descent of the pyroclastic density current (PDC) with an easting velocity of 71 m/s and a northing velocity of 29 m/s (total velocity of 76 m/s). Vertical black dashed lines indicate the different phases of activity.

easting direction and 29 m/s (104 km/hr) in the northing direction. This gives a total velocity of 76 m/s (274 m/s). This is in broad agreement with Andronico et al. (2018) who stated that the PDC had a velocity of >40 m/s (144 km/hr) and faster than the 24 November 2006 PDC which had a velocity of ~33 m/s (120 km/hr; Behncke, 2009).

6. Discussion

The results from the seismic analysis are in good agreement with the visual and geological observations. INGV-OE visual and thermal surveillance cameras observed a reddish-brown cloud expanding rapidly over the NSEC cone and down into Valle del Bove starting at 06:07:10 (Andronico et al., 2018). Similarly, the RMS amplitude of the seismic data starts to increase around 06:07:10 (Figures 3 and 4) and the source locations start trending to the east with an increasing velocity (Figure 5). By 06:08:20 the seismic source locations have returned to the NSEC, which is in agreement with the visually derived end time of the flow of ~06:08:12. Visual and seismic observations both agree on a general flow direction to the NE (Andronico et al., 2018).

The seismic source locations are also in good agreement with the PDC deposits mapped by Andronico et al. (2018), although the seismic source locations are slightly to the south and do not extend as far down flank as the mapped deposits do. The seismic source locations are in better agreement with the location of coarse-grained PDC deposits than the fine-grained PDC deposits (Figure 4). By comparison with other surficial mass movements such as debris flows and snow avalanches (Allstadt et al., 2018; Johnson et al., 2021; Marchetti et al., 2020; Watson et al., 2021; Zhang et al., 2021), PDC seismic signals are thought to be generated by the dense basal flow exerting forces on the solid Earth. Hence, the seismic-derived PDC source locations are likely to be more closely related to the coarse-grained deposits than the fine-grained deposits that are derived from the dilute cloud of hot gas and ash that surrounds the dense basal flow. Discrepancies between the location of the coarse-grained PDC deposits and seismic source locations could be due to the simplified amplitude attenuation model of geometrical spreading that does not account for complex topography and wavefield scattering. Equation 1 assumes an isotropic seismic source that, as suggested by the infrasound data, is likely not realistic for PDCs, which are spatially distributed sources that likely preferentially radiates energy in the propagation direction. This source localization method only identifies the dominant source and may miss smaller pulses of PDC activity spreading from the front of the flow or smaller PDCs when there are multiple events occurring at the same time. Future work should consider alternative algorithms that can locate multiple sources. In addition, the results may be biased by the majority of the seismic stations being located to the west of the PDC with only one station (EMFO) to the east (Figure 1).

The seismically derived velocity of 76 m/s is higher than the >40 m/s velocity estimated from visual and thermal observations by Andronico et al. (2018). Visual observations (ground-based or satellite-based), in particular, are

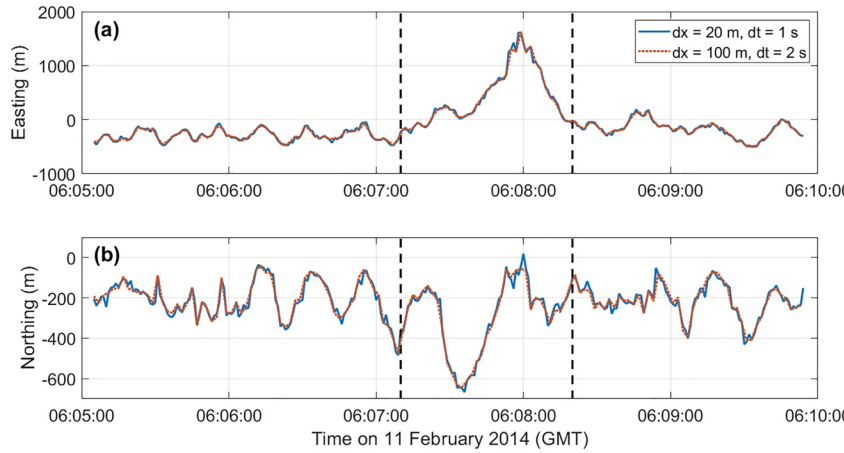

Figure 6. Comparison of mean (a) easting and (b) northing calculated using (blue, solid) 20 m grid spacing and 1 s time intervals and (red, dotted) 100 m grid spacing and 2 s time intervals.

restricted to the opaque cloud of hot gas and ash whereas the dense basal flow that we locate with the seismic data may be traveling faster within this cloud. This demonstrates the utility of combining different monitoring tools that are sensitive to different parts of the volcanic phenomena. The seismic-derived velocity is also higher than previously observed for PDCs at Mt. Etna (e.g., ∼33 m/s for the 24 November 2006 PDC; Behncke, 2009). The 11 February 2014 PDC studied here, however, was larger and traveled further (runout of 2.3 vs. 1.2 km) after reaching a much steeper area than the 2006 PDC, hence it is plausible that it had a higher velocity.

While infrasound has great utility for monitoring PDC activity (e.g., Delle Donne et al., 2014; Ripepe et al., 2009), the results shown here demonstrate the potential shortcomings of infrasound as the summit stations do not record clear PDC signals. Hence, reliable volcano monitoring benefits from using a range of tools including infrasound, seismic, visual and thermal cameras, as is done at Mt. Etna. Future work about the partitioning of seismic and acoustic energy for PDCs will be informative for characterizing flow properties, as was done by Marchetti et al. (2020) for snow avalanches.

In this work, we perform a high-resolution grid search with 20 m resolution in 2D space over the topography and calculate the source location every second. Despite the large number of grid points (∼36 million), the analysis (fitting a linear model to nine data points) is computationally simple for each grid point and, for the 5 min of data analyzed here, runs in about 10 min on a desktop computer. As the computational time is longer than the length of the data analyzed, this is not useful for real-time monitoring. The computational time could be improved by running on a faster computer or parallelizing the grid search across multiple machines. Alternatively, decreasing the spatial and temporal resolution can drastically decrease computational time. Figure 6 shows a comparison between the 20 m resolution analysis at every second with 100 m resolution at every 2 s. The results are very similar but the lower resolution result is calculated in 12 s (50x faster). This demonstrates that this analysis could be run in real-time.

INGV-OE currently uses a similar methodology to locate the source of volcanic tremors in 3D space using 30 min windows. Searching over 3D space (horizontal coordinates and depth) is important when studying tremor sources within the magma plumbing system but drastically increases the computational expense. When studying surficial mass movements such as PDCs, it is sufficient to limit the grid search to the 2D topography, which makes it tractable to perform this analysis in real-time.

Mt. Etna is a well-monitored volcano and in this work we use data from nine seismic stations located between 1 and 8 km from the summit. Previous work by Jolly et al. (2002) using a similar amplitude-based location method at Soufriere Hills volcano used between five and seven seismic stations. The majority of volcanoes, however, have fewer seismic stations. In order to demonstrate how this method performs with fewer seismic stations, we iterate over all 502 possible combinations of subsets of the seismic stations (Figure S3 in Supporting Information S1) and calculate the source location (Figures 7 and 8).

Figures 7 and 8 show that, predictably, increasing the number of seismic stations results in less variation in the source locations between different station configurations. While the results for two or three seismic stations are highly sensitive to the specific stations used, the eastward movement of the PDC is visible for four or more stations

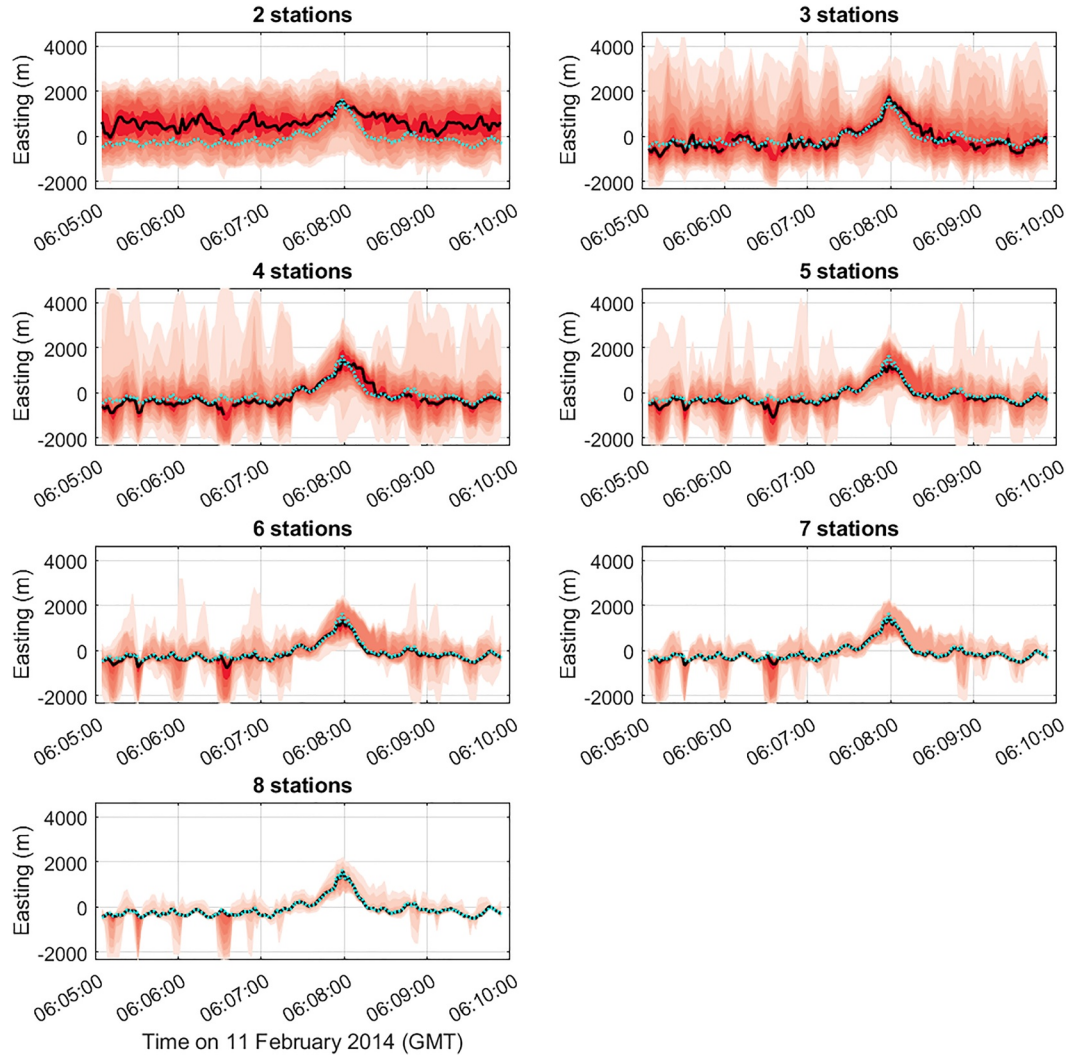

Figure 7. Easting component of median seismic source location for all possible combinations of the various subsets of seismic stations (solid black line). Shaded red regions indicate the percentiles in 5% increments between the 5th and 95th percentiles with darker red corresponding to more likely source locations. Cyan dotted line shows the solution for all nine seismic stations. The vertical extent of the axes indicates the boundaries of the search region as shown in Figure 1.

(Figure 7). These results are specific to the station locations and topography at Mt. Etna (Figure 1) but nonetheless, qualitatively show what could be achieved with various numbers of seismic stations at different volcanoes.

7. Conclusion

PDCs are hazardous and unpredictable flows that are characterized by a dense basal flow that excites seismic waves and a dilute visual-opaque cloud of hot gas and ash. PDCs are challenging to monitor, in particular because visual observations are limited to the cloud of hot gas and ash surrounding the dense basal flow. Seismic signals provide a way to track PDC movements in unparalleled spatial and temporal resolution.

Here, we present seismic and infrasound signals recorded during a PDC at Mt. Etna (Italy). We use an amplitude-based localization method (Cannata et al., 2013, 2010; Di Grazia et al., 2006) to locate the source of seismic signals before, during, and after the PDC. Before and after the PDC, seismic sources are located at NSEC whereas during the PDC the source moves downslope from NSEC and overlaps the mapped coarse-grained PDC deposits (Andronico et al., 2018). Seismic source locations are in good agreement with visual and thermal observations (Andronico et al., 2018) and we estimate the maximum PDC velocity at 76 m/s. This work demonstrates how seismic observations can provide high-resolution constraints on PDC dynamics.

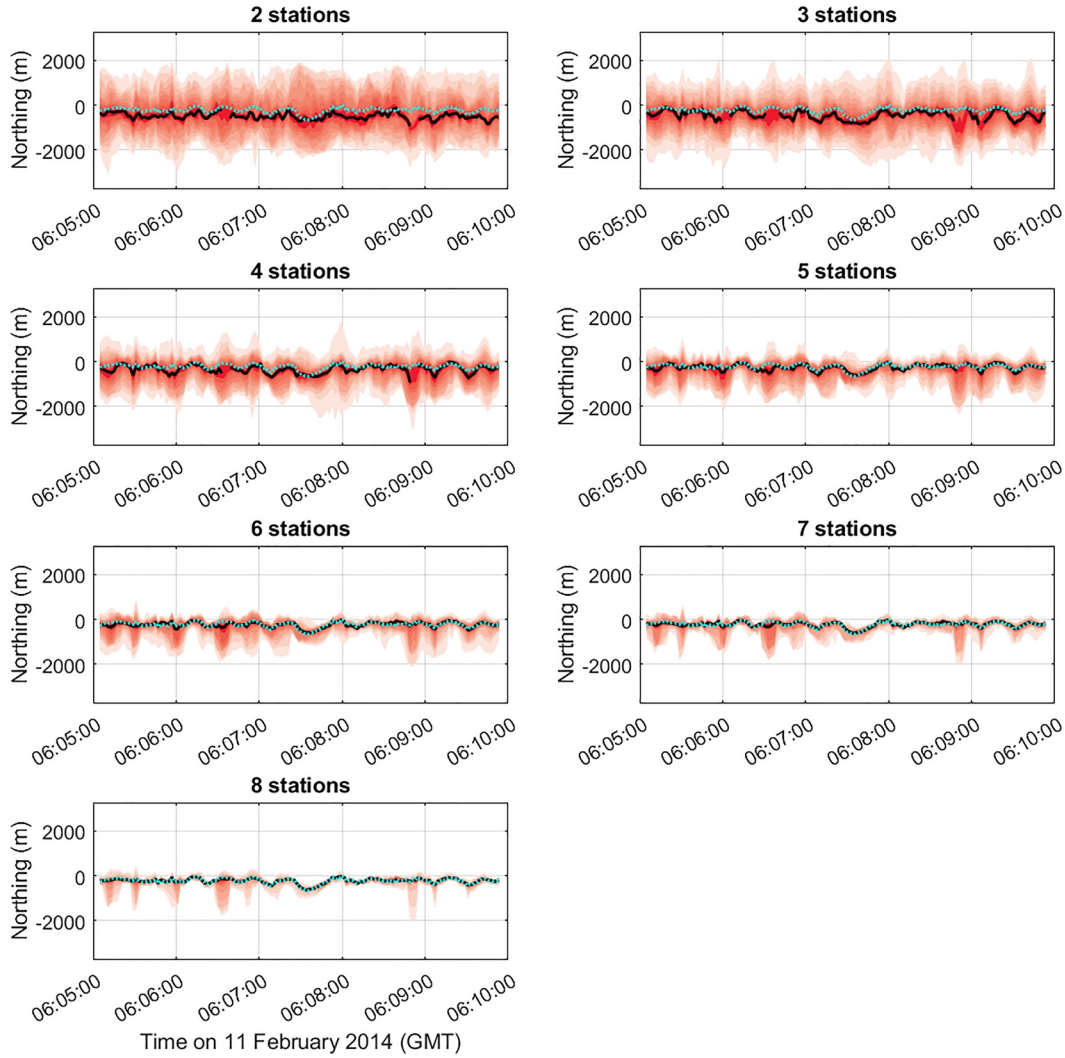

Figure 8. Northing component of median seismic source location for all possible combinations of the various subsets of seismic stations (solid black line). Shaded red regions indicate the percentiles in 5% increments between the 5th and 95th percentiles with darker red corresponding to more likely source locations. Cyan dotted line shows the solution for all nine seismic stations. The vertical extent of the axes indicates the boundaries of the search region as shown in Figure 1.

The workflow presented here could be applied to real-time to monitor PDC movements at Mt. Etna and other well-instrumented volcanoes. While this analysis is applied to a PDC, a similar amplitude-based localization approach could be used for other surficial mass movements including lahars, debris flows, and snow avalanches.

Data Availability Statement

Data and current version of the code are available at https://github.com/leighton-watson/seismicSourceLocation with the version used in this paper archived at Zenodo (https://doi.org/10.5281/zenodo.7630425). Raw data is archived at https://doi.org/10.13127/etna/side20140211.

References

Allstadt, K. E., Matoza, R. S., Lockhart, A. B., Moran, S. C., Caplan-Auerbach, J., Haney, M. M., et al. (2018). Seismic and acoustic signatures of surficial mass movements at volcanoes. *Journal of Volcanology and Geothermal Research*, *364*, 76–106. https://doi.org/10.1016/j.jvolgeores.2018.09.007

Andronico, D., Cannata, A., Di Grazia, G., & Ferrari, F. (2021). The 1986–2021 paroxysmal episodes at the summit craters of Mt. Etna: Insights into volcano dynamics and hazard. *Earth-Science Reviews*, *220*, 103686. https://doi.org/10.1016/j.earscirev.2021.103686

Acknowledgments
The authors are indebted to the technicians of the INGV, Osservatorio Etneo, for enabling the acquisition of the infrasound and seismic data and for their maintenance of the monitoring equipment. The authors thank Dr. Placido Montalto for assistance with data archiving. L.W. was supported by a Rutherford Foundation Postdoctoral Fellowship from New Zealand government funding, administered by the Royal Society Te Apārangi. A.C. thanks CHANCE project, II Edition, Università degli Studi di Catania (principal investigator A. Cannata) and grant PIACERI, 2020-22 program (PAROSSISMA project, code 22722132140; principal investigator Marco Viccaro). Open access publishing facilitated by University of Canterbury, as part of the Wiley - University of Canterbury agreement via the Council of Australian University Librarians.

Andronico, D., Di Roberto, A., De Beni, E., Behncke, B., Bertagnini, A., Del Carlo, P., & Pompilio, M. (2018). Pyroclastic density currents at Etna volcano, Italy: The 11 February 2014 case study. *Journal of Volcanology and Geothermal Research*, *357*, 92–105. https://doi.org/10.1016/j.jvolgeores.2018.04.012

Battaglia, J., Aki, K., & Ferrazzini, V. (2005). Location of tremor sources and estimation of lava output using tremor source amplitude on the Piton de la Fournaise volcano: 1. Location of tremor sources. *Journal of Volcanology and Geothermal Research*, *147*(3–4), 268–290. https://doi.org/10.1016/j.jvolgeores.2005.04.005

Behncke, B. (2009). Hazards from pyroclastic density currents at Mt. Etna (Italy). *Journal of Volcanology and Geothermal Research*, *18*(2–4), 148–160. https://doi.org/10.1016/j.jvolgeores.2008.09.021

Benage, M. C., Dufek, J., & Mothes, P. A. (2016). Quantifying entrainment in pyroclastic density currents from the Tungurahua eruption, Ecuador: Integrating field proxies with numerical simulations. *Geophysical Research Letters*, *43*(13), 6932–6941. https://doi.org/10.1002/2016GL069527

Breard, E. C. P., & Lube, G. (2017). Inside pyroclastic density currents - uncovering the enigmatic flow structure and transport behavior in large-scale experiments. *Earth and Planetary Science Letters*, *458*, 22–36. https://doi.org/10.1016/J.EPSL.2016.10.016

Calder, E. S., Luckett, R., Sparks, R. S. J., & Voight (2002). *Mechanisms of lava dome instability and generation of rockfalls and pyroclastic flows at Soufriere Hills Volcano, Montserrat* (Vol. 21, pp. 173–190). Geological Society. https://doi.org/10.1144/GSL.MEM.2002.021.01.08

Calvari, S., Di Traglia, F., Ganci, G., Giudicepietro, F., Macedonio, G., Cappello, A., et al. (2020). Overflows and pyroclastic density currents in March–April 2020 at Stromboli volcano detected by remote sensing and seismic monitoring data. *Remote Sensing*, *12*(18), 3010. https://doi.org/10.3390/rs12183010

Cannata, A., Di Grazia, G., Aliotta, M., Cassisi, C., Montalto, P., & Patanè, D. (2013). Monitoring seismo-volcanic and infrasonic signals at volcanoes: Mt. Etna case study. *Pure and Applied Geophysics*, *170*(11), 1751–1771. https://doi.org/10.1007/s00024-012-0634-x

Cannata, A., Di Grazia, G., Montalto, P., Ferrari, F., Nunnari, G., Patanè, D., & Privitera, E. (2010). New insights into banded tremor from the 2008–2009 Mount Etna eruption. *Journal of Geophysical Research*, *115*(B12), B12318. https://doi.org/10.1029/2009JB007120

Cioni, R., Gurioli, L., Lanza, R., & Zanella, E. (2004). Temperatures of the A.D. 79 pyroclastic density current deposits (Vesuvius, Italy). *Journal of Geophysical Research: Solid Earth*, *109*(B2), B02207. https://doi.org/10.1029/2002JB002251

Cole, P. D., Calder, E. S., Sparks, R. S. J., Clarke, A. B., Druitt, T. H., Young, S. R., et al. (2002). *Deposits from dome-collapse and fountain-collapse pyroclastic flows at Soufrière Hills Volcano, Montserrat* (Vol. 21, pp. 231–262). Geological Society. https://doi.org/10.1144/gsl.mem.2002.021.01.11

De Angelis, S., Bass, V., Hards, V., & Ryan, G. (2007). Seismic characterization of pyroclastic flow activity at Soufrière Hills Volcano, Montserrat, 8 January 2007. *Natural Hazards Earth System Science*, *7*(4), 467–472. https://doi.org/10.5194/nhess-7-467-2007

Delle Donne, D., Ripepe, M., De Angelis, S., Cole, P. D., Lacanna, G., Poggi, P., & Stewart, R. (2014). *Thermal, acoustic and seismic signals from pyroclastic density currents and Vulcanian explosions at Soufriere Hills Volcano, Montserrat* (pp. 169–178). Geological Society. https://doi.org/10.1144/M39.9

DeRoin, N., McNutt, S. R., Sentman, D. D., & Reyes, C. (2012). Seismicity of block-and-ash flows occurring during the 2006 eruption of Augustine Volcano, Alaska. *Journal of Volcanology and Geothermal Research*, *213–214*, 14–26. https://doi.org/10.1016/j.jvolgeores.2011.10.007

Di Grazia, G., Falsaperla, S., & Langer, H. (2006). Volcanic tremor location during the 2004 Mount Etna lava effusion. *Geophysical Research Letters*, *33*(4), L04304. https://doi.org/10.1029/2005GL025177

Doronzo, D. M., Valentine, G. A., Dellino, P., & de Tullio, M. D. (2010). Numerical analysis of the effect of topography on deposition from dilute pyroclastic density currents. *Earth and Planetary Science Letters*, *300*(1–2), 164–173. https://doi.org/10.1016/J.EPSL.2010.10.003

Druitt, T. H. (1998). Pyroclastic density currents. In J. S. Gilbert, & R. S. J. Sparks (Eds.), *The physics of explosive volcanic eruptions* (Vol. 145, pp. 145–182). Geological Society, London, Special Publications. https://doi.org/10.1144/GSL.SP.1996.145.01.08

Dufek, J. (2016). The fluid mechanics of pyroclastic density currents. *Annual Reviews of Fluid Mechanics*, *48*(1), 459–485. https://doi.org/10.1146/annurev-fluid-122414-034252

Dufek, J., & Bergantz, G. W. (2007a). Dynamics and deposits generated by the Kos Plateau Tuff eruption: Controls of basal particle loss on pyroclastic flow transport. *Geochemistry, Geophysics, Geosystems*, *8*(12), Q12007. https://doi.org/10.1029/2007GC001741

Dufek, J., & Bergantz, G. W. (2007b). Suspended load and bed-load transport of particle-laden gravity currents: The role of particle-bed interaction. *Theoretical and Computational Fluid Dynamics*, *21*(2), 119–145. https://doi.org/10.1007/s00162-007-0041-6

Dufek, J., Esposti Ongaro, T., & Roche, O. (2009). Pyroclastic density currents: Processes and models. In *Modeling volcanic processes: The physics and mathematics of volcanism* (pp. 203–229). https://doi.org/10.1017/CBO9781139021562.010

Fisher, R. V. (1966). Mechanisms of deposition from pyroclastic flows. *American Journal of Science*, *264*(5), 350–363. https://doi.org/10.1007/BF01078808

Fisher, R. V. (1979). Models for pyroclastic surges and pyroclastic flows. *Journal of Volcanology and Geothermal Research*, *6*(3–4), 305–318. https://doi.org/10.1016/0377-0273(79)90008-8

Fisher, R. V., Orsi, G., Ort, M., & Heiken, G. (1993). Mobility of a large-volume pyroclastic flow—Emplacement of the Campanian ignimbrite, Italy. *Journal of Volcanology and Geothermal Research*, *56*(3), 205–220. https://doi.org/10.1016/0377-0273(93)90017-L

Fujii, T., & Nakata, S. (1999). The 15 September 1991 pyroclastic flows at Unzen volcano (Japan): A flow model for associated ash-cloud surges. *Journal of Volcanology and Geothermal Research*, *89*(1–4), 159–172. https://doi.org/10.1016/S0377-0273(98)00130-9

Ganci, G., Cappello, A., Bilotta, G., Hérault, A., Zago, V., & Del Negro, C. (2019). Digital Elevation Model of Mt Etna updated to 18 December 2015, supplement to: Ganci, Gaetana; Cappello, Annalisa; Bilotta, Giuseppe; Hérault, Alexis; Zago, Vito; Del Negro, Ciro (2018): Mapping Volcanic Deposits of the 2011–2015 Etna Eruptive Events Using Satellite Remote Sensing. Frontiers in Earth Science, 6:83 [Dataset]. PANGAEA - Data Publisher for Earth & Environmental Science. https://doi.org/10.1594/pangaea.899140

Guriol, L., Sulpizio, R., Cioni, R., Sbrana, A., Santacroce, R., Luperini, W., & Andronico, D. (2010). Pyroclastic flow hazard assessment at Somma-Vesuvius based on the geological record. *Bulletin of Volcanology*, *72*(9), 1021–1038. https://doi.org/10.1007/s00445-010-0379-2

Instituto Nazionale di Geofisica e Vulcanologia (INGV) Osservatorio Etneo. (2014). Report on the landslide of 11 February 2014 at the New Southeast Crater of Etna and on the pyroclastic flow generated.

Instituto Nazionale di Geofisica e Vulcanologia (INGV) Osservatorio Etneo. (2020a). Bollettino settimanale 7 December 2020 to 13 December 2020. Rep. N = 51/2020. Retrieved from https://www.ct.ingv.it/index.php/monitoraggio-e-sorveglianza/prodotti-del-monitoraggio/bollettini-settimanali-multidisciplinari/400-bollettino-settimanale-sul-monitoraggio-vulcanico-geochimico-e-sismico-del-vulcano-etna-del-15-12-2020/file

Instituto Nazionale di Geofisica e Vulcanologia (INGV) Osservatorio Etneo. (2020b). Bollettino settimanale sul monitoraggio vulcanico, geochimico e sismico del vulcano Etna. 23 November 2020 to 29 November 2020. Rep. N = 49/2020. Retrieved from https://www.ct.ingv.it/index.php/monitoraggio-e-sorveglianza/prodotti-del-monitoraggio/bollettini-settimanali-multidisciplinari/394-bollettino-settimanale-sul-monitoraggio-vulcanico-geochimico-e-sismico-del-vulcano-etna20201201/file

Instituto Nazionale di Geofisica e Vulcanologia (INGV) Osservatorio Etneo. (2022). Bollettino settimanale 7 February 2022 to 13 February 2022. Rep.*N*=07/2022ETNA.Retrievedfromhttps://www.ct.ingv.it/index.php/monitoraggio-e-sorveglianza/prodotti-del-monitoraggio/bollettini-settimanali-multidisciplinari/601-bollettino-settimanale-sul-monitoraggio-vulcanico-geochimico-e-sismico-del-vulcano-Etna-del-2022-02-15/file

Johnson, J. B., Anderson, J. F., Marshall, H. P., Havens, S., & Watson, L. M. (2021). Snow avalanche detection and source constraints made using a networked array of infrasound sensors. *Journal of Geophysical Research Earth Surface*, *126*(3). https://doi.org/10.1029/2020JF005741

Jolly, A. D., Thompson, G., & Norton, G. E. (2002). Locating pyroclastic flows on Soufriere Hills Volcano, Montserrat, West Indies, using amplitude signals from high dynamic range instruments. *Journal of Volcanology and Geothermal Research*, *118*(3–4), 299–317. https://doi.org/10.1016/S0377-0273(02)00299-8

Larocca, G., Scuderi, L., Di Prima, S., & Cannata, A. (2023). Seismic and infrasonic data recorded at Mt. Etna on 11 February 2014 (SIDE2014) [Dataset]. https://doi.org/10.13127/etna/side20140211

Lube, G., Breard, E. C. P., Jones, J., Fullard, L., Dufek, J., Cronin, S. J., & Wang, T. (2019). Generation of air lubrication within pyroclastic density currents. *Nature Geoscience*, *12*(5), 381–386. https://doi.org/10.1038/s41561-019-0338-2

Marchetti, E., Van Herwijnen, A., Christen, M., Silengo, M. C., & Barfucci, G. (2020). Seismo-acoustic energy partitioning of a powder snow avalanche. *Earth Surface Dynamics*, *8*(2), 399–411. https://doi.org/10.5194/esurf-8-399-2020

Moore, J. G., & Rice, C. J. (1984). *Chronology and character of the 18 May 1980, explosive eruptions of Mount Saint Helens, explosive volcanism: Inception, evolution, and hazards* (Vol. 10, pp. 133–157). National Academy Press.

Neri, A., Esposti Ongaro, T., Macedonio, G., & Gidaspow, D. (2003). Multiparticle simulation of collapsing volcanic columns and pyroclastic flow. *Journal of Geophysical Research*, *108*(B4), 2202. https://doi.org/10.1029/2001JB000508

Norini, G., De Beni, E., Andronico, D., Polacci, M., Burton, M., & Zucca, F. (2009). The 16 November 2006 flank collapse of the south-east crater at Mount Etna, Italy: Study of the deposit and hazard assessment. *Journal of Geophysical Research: Solid Earth*, *114*(B2), B02204. https://doi.org/10.1029/2008JB005779

Patanè, D., Di Grazia, G., Cannata, A., Montalto, P., & Boschi, E. (2008). The shallow magma pathway geometry at Mt. Etna volcano. *Geochemistry, Geophysics, Geosystems*, *9*(12), Q12021. https://doi.org/10.1029/2008GC002131

Pollock, N. M., Brand, B. D., Rowley, P. J., Sarocchi, D., & Sulpizio, R. (2019). Inferring pyroclastic density current flow conditions using syn-depositional sedimentary structures. *Bulletin of Volcanology*, *81*(8), 46. https://doi.org/10.1007/s00445-019-1303-z

Ripepe, M., De Angelis, S., Lacanna, G., Poggi, P., Williams, C., Marchetti, E., et al. (2009). Tracking pyroclastic flows at Soufrière Hills volcano. *EOS*, *90*(27), 229–236. https://doi.org/10.1029/2009eo270001

Roche, O., Montserrat, S., Niño, Y., & Tamburrino, A. (2010). Pore fluid pressure and internal kinematics of gravitational laboratory air-particle flows: Insights into the emplacement dynamics of pyroclastic flows. *Journal of Geophysical Research*, *115*(B9), B09206. https://doi.org/10.1029/2009JB007133

Smith, R. L. (1960). Ash flows. *Bulletin of the Geological Society of America*, *71*(6), 795–842. https://doi.org/10.1130/0016-7606(1960)71[795:AF]2.0.CO;2

Sparks, R. S. J., Self, S., & Walker, G. P. L. (1973). Products of ignimbrite eruptions. *Geology*, *1*(3), 115–118. https://doi.org/10.1130/0091-7613(1973)1<115:POIE>2.0.CO;2

Takahashia, T., & Tsujimoto, H. (2000). A mechanical model for Merapi-type pyroclastic flow. *Journal of Volcanology and Geothermal Research*, *98*(1–4), 91–115. https://doi.org/10.1016/S0377-0273(99)00193-6

Uhira, K., Yamasato, H., & Takeo, M. (1994). Source mechanism of seismic waves excited by pyroclastic flows observed at Unzen volcano.

Valentine, G. A., Buesch, D. C., & Fisher, R. V. (1989). Basal layered deposits of the Peach Springs Tuff, northwestern Arizona, USA. *Bulletin of Volcanology*, *51*(6), 395–414. https://doi.org/10.1007/BF01078808

Valentine, G. A., & Wohletz, K. H. (1989). Numerical models of Plinian eruption columns and pyroclastic flows. *Journal of Geophysical Research*, *94*(B2), 1867–1887. https://doi.org/10.1029/JB094iB02p01867

Walker, G. P. L. (1971). Grain-size characteristics of pyroclastic deposits. *The Journal of Geology*, *79*(6), 696–714. https://doi.org/10.1086/627699

Walter, F., Burtin, A., McArdell, B. W., Hovius, N., Weder, B., & Turowski, J. M. (2017). Testing seismic amplitude source location for fast debris-flow detection at Illgraben, Switzerland. *Natural Hazards and Earth System Science*, *17*(6), 939–955. https://doi.org/10.5194/nhess-17-939-2017

Watson, L. M., Carpenter, B., Thompson, K., & Johnson, J. B. (2021). Using local infrasound arrays to detect plunging snow avalanches along the Milford Road, New Zealand (Aotearoa). *Natural Hazards*, *111*(1), 949–972. https://doi.org/10.1007/s11069-021-05086-w

Wilson, C. J. N. (1980). The role of fluidization in the emplacement of pyroclastic claws: An experimental approach. *Journal of Volcanology and Geothermal Research*, *8*(2–4), 231–249. https://doi.org/10.1016/0377-0273(80)90106-7

Woods, A. W., Bursik, M. I., & Kurbatov, A. V. (1998). The interaction of ash flows with ridges. *Bulletin of Volcanology*, *60*(1), 38–51. https://doi.org/10.1007/s004450050215

Yamasato, H. (1997). Quantitative analysis of pyroclastic flows using infrasonic and seismic data at Unzen volcano, Japan. *Journal of Physics of the Earth*, *45*(6), 397–416. https://doi.org/10.4294/jpe1952.45.397

Zhang, Z., Walter, F., McArdell, B. W., Wenner, M., Chmiel, M., de Haas, T., & He, S. (2021). Insights from the particle impact model into the high-frequency seismic signature of debris flows. *Geophysical Research Letters*, *48*(1). https://doi.org/10.1029/2020GL088994

Zobin, V. M. (2018). Development of the 10–11 July 2015 two-stage sequence of multiple emplacements of pyroclastic density currents at Volcán de Colima, México: Insight from associated seismic signals. *Journal of Volcanology and Geothermal Research*, *351*, 29–40. https://doi.org/10.1016/j.jvolgeores.2017.12.012

Zobin, V. M., Plascencia, I., Reyes, G., & Navarro, C. (2009). The characteristics of seismic signals produced by lahars and pyroclastic flows: Volcán de Colima, México. *Journal of Volcanology and Geothermal Research*, *179*(1–2), 157–167. https://doi.org/10.1016/j.jvolgeores.2008.11.001